ACS APPLIED MATERIALS & INTERFACES

www.acsami.org Research Article

Thermal Conductivity of Aluminum Scandium Nitride for 5G Mobile Applications and Beyond

Yiwen Song, Carlos Perez, Giovanni Esteves, James Spencer Lundh, Christopher B. Saltonstall, Thomas E. Beechem, Jung In Yang, Kevin Ferri, Joseph E. Brown, Zichen Tang, Jon-Paul Maria, David W. Snyder, Roy H. Olsson III, Benjamin A. Griffin, Susan E. Trolier-McKinstry, Brian M. Foley, and Sukwon Choi*

Cite This: *ACS Appl. Mater. Interfaces* 2021, 13, 19031−19041

Read Online

ACCESS | Metrics & More | Article Recommendations

ABSTRACT: Radio frequency (RF) microelectromechanical systems (MEMS) based on $Al_{1-x}Sc_xN$ are replacing AlN-based devices because of their higher achievable bandwidths, suitable for the fifth-generation (5G) mobile network. However, overheating of $Al_{1-x}Sc_xN$ film bulk acoustic resonators (FBARs) used in RF MEMS filters limits power handling and thus the phone's ability to operate in an increasingly congested RF environment while maintaining its maximum data transmission rate. In this work, the ramifications of tailoring of the piezoelectric response and microstructure of $Al_{1-x}Sc_xN$ films on the thermal transport have been studied. The thermal conductivity of $Al_{1-x}Sc_xN$ films (3−8 W m^{-1} K^{-1}) grown by reactive sputter deposition was found to be orders of magnitude lower than that for *c*-axis-textured AlN films due to alloying effects. The film thickness dependence of the thermal conductivity suggests that higher frequency FBAR structures may suffer from limited power handling due to exacerbated overheating concerns. The reduction of the abnormally oriented grain (AOG) density was found to have a modest effect on the measured thermal conductivity. However, the use of low AOG density films resulted in lower insertion loss and thus less power dissipated within the resonator, which will lead to an overall enhancement of the device thermal performance.

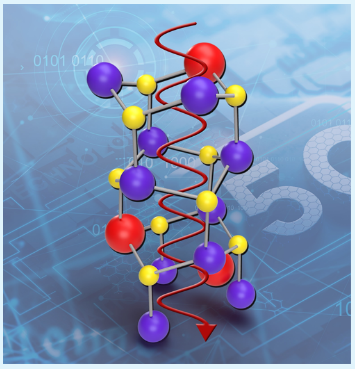

KEYWORDS: *aluminum scandium nitride, frequency-domain thermoreflectance, thermal conductivity, time-domain thermoreflectance, phonon transport, radio frequency acoustic filters, scandium aluminum nitride*

1. INTRODUCTION

To meet the ultrawide bandwidth requirements for fifth-generation (5G) mobile phones,[1,2] manufacturers have recently adopted scandium aluminum nitride ($Al_{1-x}Sc_xN$; x is the Sc composition), a wurtzite-structured solid solution, as the piezoelectric in film bulk acoustic resonators (FBARs). The interest in replacing aluminum nitride (AlN) FBARs [used in some 4G mobile phone radio frequency (RF) duplexers] with $Al_{1-x}Sc_xN$ FBARs originates from the enhancement of electromechanical coupling (k_t^2), which scales indirectly with the piezoelectric coefficient d_{33}. The d_{33} of $Sc_xAl_{1-x}N$ has been predicted to reach a value five times larger than that for AlN at $x = 0.43$.[3] This dramatic enhancement of d_{33} and the complementary metal-oxide-semiconductor (CMOS) process-compatibility facilitates the development of 5G mobile phone duplexers[1,4−6] with wide bandwidth[7−9] and low insertion loss.[7,8] These intrinsic advantages are, in turn, motivating significant research aimed at achieving high k_t^2 and quality factor (Q), simultaneously.

However, for an FBAR to handle the high operational frequencies of the 5G mobile network, its physical dimensions typically decrease, and higher RF input powers are required to counter signal attenuation. Higher power and smaller size translate into an increased operational heat flux. This higher heat flux, meanwhile, occurs within a solid solution ($Al_{1-x}Sc_xN$) that will have a greatly reduced thermal conductivity relative to the AlN material that it replaces. Furthermore, the FBAR structure itself is prone to overheating because the piezoelectric film is typically released from the substrate, which severely limits the thermal pathway for heat dissipation. $Al_{1-x}Sc_xN$ resonators exhibit a 50% larger resonant frequency drift with temperature rise[10] than their AlN counterparts.[11,12] Self-heating in $Sc_xAl_{1-x}N$ FBARs can, in principle, constrain the maximum transmission rate, and if allowed to proceed unchecked, may cause thermal failure.[7,12,13] Despite the thermal implications on performance, fundamental

Received: February 11, 2021
Accepted: April 2, 2021
Published: April 14, 2021

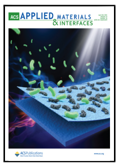

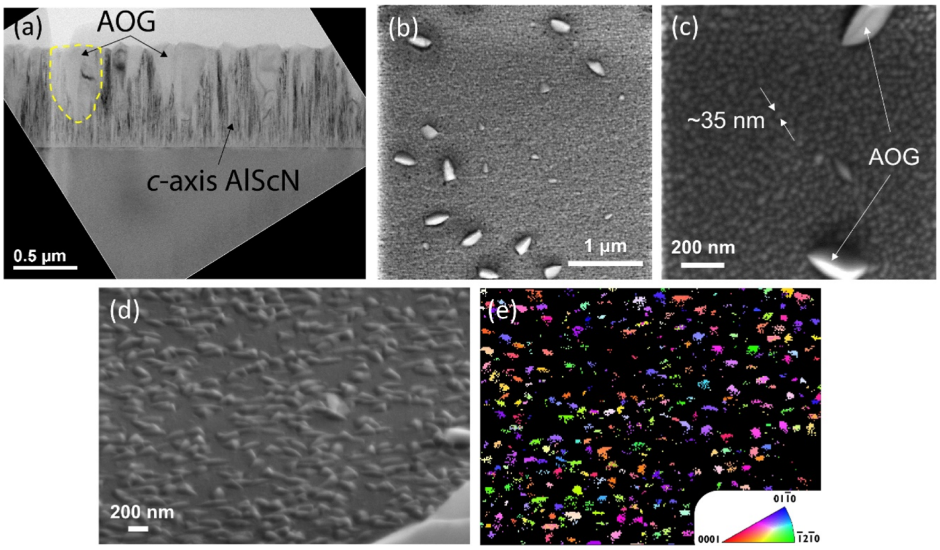

Figure 1. (a) TEM cross-section of an $Al_{0.875}Sc_{0.125}N$ film showing AOGs and their propagation through the film thickness. (b) 75*k*× and (c) 200*k*× plan-view SEM images of an $Al_{0.8}Sc_{0.2}N$ film showing the primary *c*-axis-oriented grain structure as well as AOGs. (d) 750 nm thick $Al_{0.8}Sc_{0.2}N$ film with a high density of AOGs, and (e) inverse-pole figure, gathered from EBSD, that maps the orientation of AOGs from the film normal direction (*Z*-direction). EBSD results show no strong preferred orientation for the AOGs.

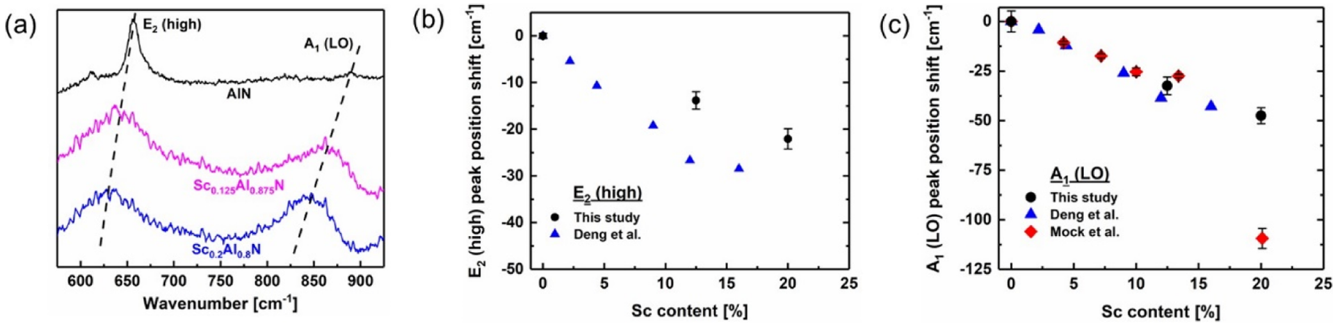

Figure 2. (a) Background subtracted Raman spectra of AlN, $Sc_{0.125}Al_{0.875}N$, and $Sc_{0.2}Al_{0.8}N$ films. The dashed lines qualitatively show the redshift of the E_2 (high) and A_1 (LO) modes as the Sc content in the films is increased. (b) Shift of the E_2 (high) phonon frequency (peak position) as a function of the Sc content from this study and Deng et al.[21] (c) Shift of the A_1 (LO) phonon frequency as a function of the Sc content from this study, Deng et al.,[21] and Mock et al.[22]

investigations of the thermal transport processes that govern heat dissipation in $Al_{1-x}Sc_xN$ remain lacking.

In response, this work reports how changes in the alloy composition, thickness, and microstructure influence the thermal conductivity of $Al_{1-x}Sc_xN$. Specifically, we measure the variation in $Al_{1-x}Sc_xN$ thermal conductivity for films synthesized via reactive sputter deposition as a function of Sc composition, film thickness, temperature, and the concentration of abnormally oriented grains (AOGs). Through this examination, the design trade-offs associated with this material, in terms of attempting to optimize both the device acousto-electric performance and the ability to dissipate heat, are identified. In particular, it is shown that several phonon scattering mechanisms associated with solid solution (i.e., phonon-alloy/disorder scattering), grain boundaries, and film surfaces drive a substantial thermal conductivity reduction relative to AlN. Device engineers must therefore grapple with the necessity of designing cooling solutions enabling the use of a low thermal conductivity material (<10 W m^{-1} K^{-1}) operating within the envelope of 5G requirements.

2. RESULTS AND DISCUSSION

2.1. AlN and $Al_{1-x}Sc_xN$ Film Description. Polycrystalline AlN and $Al_{1-x}Sc_xN$ films with compositions of $x = 0$, 0.125, and 0.20 were deposited via reactive sputter deposition on 6″ Si ⟨100⟩ substrates using pulsed-DC magnetron sputtering, following previous reports.[14] Deposition conditions for the $Al_{1-x}Sc_xN$ films were 5 kW of power on the single-alloy target, an Ar/N_2 gas flow of 25/125 sccm, and a platen temperature of 375 °C. For AlN growth, a platen temperature of 350 °C and an Ar/N_2 gas flow of 20/80 sccm were employed. The film stress was controlled using substrate bias, which applies RF power to the substrate during deposition to increase the compressive stress of the film.[15,16] The film thickness range used in this study was 50−1000 nm, while the stress ranged from −1700 to −5.7 MPa. These stress values were determined via wafer curvature measurements.[17] As reported elsewhere, the density of AOGs tended to be lower in films with higher substrate bias.[18]

Figure 1 shows representative transmission electron microscopy (TEM) and scanning electron microscopy (SEM) images. As shown in Figure 1c, the columnar grain size of the *c*-axis-textured AlN and $Al_{1-x}Sc_xN$ films were approximately 35 nm across in all samples. The AOGs observed in the Al$_{1-x}$Sc$_x$N films had lateral sizes of 50−250 nm. The degree of *c*-axis orientation was characterized with X-ray diffraction by measuring the rocking curve of the {0002} reflection of the Al$_{1-x}$Sc$_x$N film. Correlation between the rocking curve measurement of various AlN films and the electromechanical coupling coefficient (k_t^2) has shown that films with smaller rocking curve linewidths (full width at half-maximum, FWHM) exhibit high k_t^2.[19] Therefore, Al$_{1-x}$Sc$_x$N films with rocking curve measurements ≤2° should be used to achieve high k_t^2.[20] In this study, films with a thickness greater than 400 nm showed a FWHM less than 2°.

The presence of AOGs lowers the crystallographic texture of Al$_{1-x}$Sc$_x$N films. Figure 1c illustrates AOGs on the Al$_{0.8}$Sc$_{0.2}$N film that protrude out of the *c*-axis-oriented matrix. As shown in the electron backscattering diffraction (EBSD) data (Figure 1e) of Figure 1d, for an Al$_{0.8}$Sc$_{0.2}$N film with a high density of AOGs, there is no preferred orientation for the AOGs.

Raman spectroscopy was employed to qualitatively assess changes in the phonon energies and scattering rates that were induced with the incorporation of scandium. Using this approach, Figure 2a presents the difference in Raman spectra between the Si wafer coated with Al$_{1-x}$Sc$_x$N and the bare Si substrate where modes associated with the E$_2$ (high) (635−660 cm^{-1}) and A$_1$(LO) (825−850 cm^{-1}) of Al$_{1-x}$Sc$_x$N are clearly observed. The incorporation of scandium causes a redshift and broadening of the Raman modes indicating a softening of the lattice and an increased scattering rate of the optical phonons. Each change is associated with a reduction in thermal conductivity. Softening, for example, is seen in the redshift of the E$_2$ (high) and A$_1$ (LO) mode peak positions to lower wavenumbers with additional Sc content (Figure 2a). Figure 2b,c quantifies the concentration-dependent shift, which is similar to those reported previously by Deng et al.[21] and Mock et al.[22] Phenomenologically, Sc incorporation promotes softening because the average atomic mass of the oscillators increases and the bond covalency drops.[21] Both effects reduce thermal conductivity.

The scattering rate of the optical modes increases with Sc content as well, as indicated by the broadening of the Raman modes in Figure 2a with additional scandium. Quantitatively, as shown in Table 1, the linewidth of the E$_2$ (high) mode increases with increasing Sc content from 15.6 cm^{-1} for AlN to 61.5 cm^{-1} for Al$_{0.8}$Sc$_{0.2}$N. This suggests much more disruption in the period potential due to solid solution. Owing to the time−uncertainty relation,[23] in which scattering time is inversely proportional to FWHM, this implies a reduction of the scattering time of the optical phonon modes by a factor of nearly 4. Reductions in the scattering time of phonons, in turn, imply a lessening in the thermal conductivity.

Table 1. Peak Position and Linewidth (FWHM) of the E$_2$ (High) Phonon Mode of Sc$_x$Al$_{1-x}$N Films with ∼730−820 nm[b] Thicknesses[a]

Sc content [%]	0 (AlN)	12.5	20
peak position [cm^{-1}]	657.1 ± 0.4[b] 658[c] 657[d]	643.2 ± 1.8[b] 628.9[c]	635 ± 2.1[b] 611.4[c]
FWHM [cm^{-1}]	15.6[b]	52.3[b]	61.5[b]

[a] Data reported in this study were based on an average of 100 measurements. [b] This study. [c] Calculated using linear fit parameters reported by Deng et al.[21] [d] Value reported for unstrained AlN at 300 K.[24]

2.2. Thermal Characterization Results.

Thermal conductivity measurements of *c*-axis-textured AlN and Al$_{1-x}$Sc$_x$N films with various Sc compositions (x = 0.125 and 0.2) and two different thicknesses (∼110 and ∼760 nm) were performed using time-domain thermoreflectance (TDTR)[25] and frequency-domain thermoreflectance (FDTR) techniques.[26] This cross-validation was conducted to rule out potential sources of error and reduce uncertainty due to the complementary sensitivities of the two techniques.[27]

As shown in Figure 3a, for Al$_{1-x}$Sc$_x$N with x = 0.125 and 0.2 and a film thickness of ∼760 nm, the measured cross-plane thermal conductivities (κ) were ∼7.4 and ∼4.8 W m^{-1} K^{-1}, respectively (the actual thicknesses for the AlN, Al$_{0.875}$Sc$_{0.125}$N, and Al$_{0.8}$Sc$_{0.2}$N films are 733, 765, and 816 nm, respectively, as measured by spectroscopic ellipsometry). These values are an order of magnitude lower than that for the AlN film with a similar thickness and microstructure (∼51 W m^{-1} K^{-1}) and 2 orders of magnitude lower than a single-crystal epitaxial film of AlN (∼320 W m^{-1} K^{-1}).[28] It should be noted that the average columnar (lateral) grain size resulting from the reactive sputter deposition process[18,29] was consistent (∼35 nm; Figure 1c) among all the AlN and Al$_{1-x}$Sc$_x$N films investigated in this work. Consequently, from a practical perspective, the reduction in thermal conductivity underscores the intrinsic trade-off between piezoelectric and thermal performance in the Al$_{1-x}$Sc$_x$N solid solution.

This large reduction in κ in moving from AlN to Al$_{1-x}$Sc$_x$N films is attributed to increased phonon scattering that is primarily due to phonon-alloy disorder scattering.[30] The significantly increased phonon scattering rate is also manifested by the broadening of the linewidth of the Raman active phonon modes of the Al$_{0.875}$Sc$_{0.125}$N and Al$_{0.8}$Sc$_{0.2}$N films compared to those for AlN, as shown in Figure 2 and Table 1.[24,31]

Alloying has an acute effect on the κ of Al$_{1-x}$Sc$_x$N because of the lattice disruption associated with alloying AlN (wurtzite) with ScN (rocksalt). To quantify, the κ of Al$_{0.8}$Sc$_{0.2}$N (∼4.8 W m^{-1} K^{-1}) is ∼36% lower than that of Al$_{0.875}$Sc$_{0.125}$N (∼7.4 W m^{-1} K^{-1}) for films with a thickness of ∼760 nm. In contrast, previous work examining the wurtzite phase isostructural alloy Al$_{1-x}$Ga$_x$N with identical characterization methods found that a similar reduction in κ (35%) required a much larger variation in composition from x ∼ 0.1 to ∼0.5.[32] Mechanistically, the large reduction in the κ of Al$_{1-x}$Sc$_x$N as compared to Al$_{1-x}$Ga$_x$N can be attributed to the evolution in bond characteristics[33] of the solid solution with increasing x. Increasing x in Al$_{1-x}$Sc$_x$N solid solutions results in an increased displacement of the Al/Sc atoms along the *c*-axis.[33] This results in a reduction of the elastic stiffness constant C_{33} and a nonlinear enhancement of the piezoelectric stress constant e_{33}.[4,34] Accordingly, as Sc content approaches the critical concentration x_c at which phase separation occurs, significant increases are observed in both the piezoelectric modulus d_{33} ($\sim e_{33}/C_{33}$) and the electromechanical coupling coefficient k_t^2 ($=e_{33}^2/[(C_{33} + e_{33}^2/\varepsilon_{33})\varepsilon_{33}]$).[4] The lattice softening[11] with increasing x lowers the group velocities of the acoustic phonons that dominate κ. Thus, it is anticipated that Al$_{1-x}$Sc$_x$N (in the wurtzite phase) will continue to exhibit a nonlinear reduction in κ as x approaches x_c, whereas d_{33} is maximized.

Despite being dominated by alloy scattering, size effects are also evident in the thermal response of the Al$_{1-x}$Sc$_x$N. As

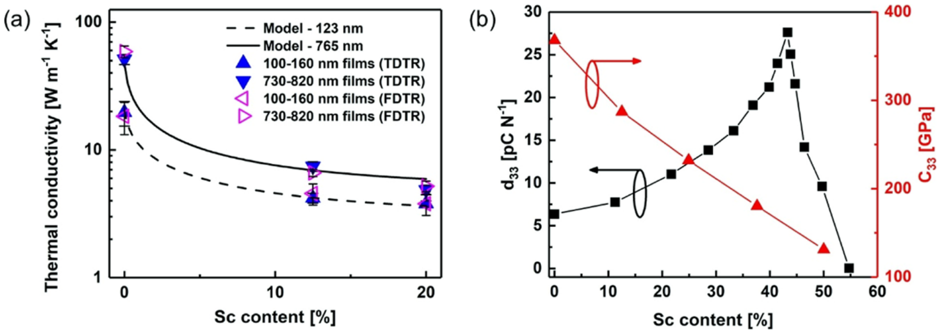

Figure 3. (a) Compositional dependence of $Al_{1-x}Sc_xN$ thermal conductivity obtained from TDTR/FDTR measurements and virtual crystal approximation (VCA) simulation (to be discussed in the "Thermal Modeling Results" section). (b) Evolution of the piezoelectric modulus d_{33} (from ref 35) and elastic stiffness constant C_{33} (from ref 34).

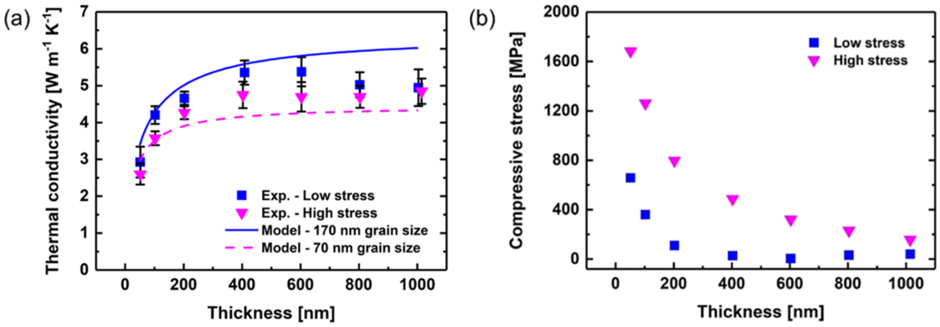

Figure 4. (a) Thickness dependence of the thermal conductivity of $Al_{0.8}Sc_{0.2}N$ films. (b) Residual stress in the two series of the $Al_{0.8}Sc_{0.2}N$ films (low stress vs high stress) as a function of layer thickness (to be discussed in the "Thermal Modeling Results" section).

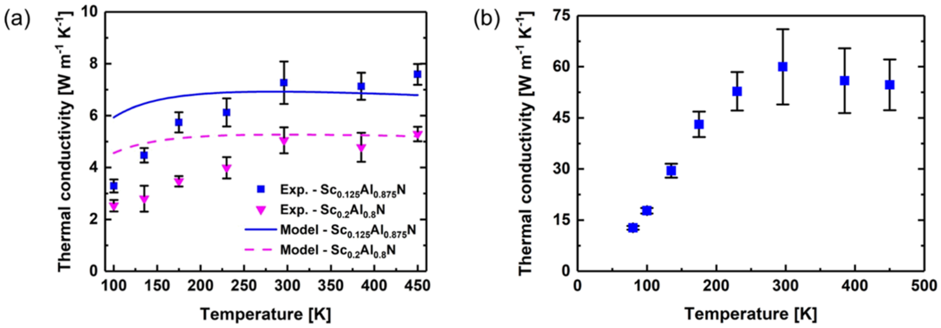

Figure 5. (a) Temperature-dependent thermal conductivity of the ~760 nm thick $Al_{1-x}Sc_xN$ (x = 0.125 and 0.2) films. (b) Also shown is the AlN film thermal conductivity as a function of temperature.

shown in Figure 3a, κ is observed to decrease over all Sc compositions as the thickness of the films decreases from ~760 to ~110 nm (the actual thicknesses for the AlN, $Al_{0.875}Sc_{0.125}N$, and $Al_{0.8}Sc_{0.2}N$ films are 157, 107, and 105 nm, respectively). When the film thickness of a crystallite becomes comparable to the mean-free path of phonons, incoherent phonon-boundary scattering will impact κ.[36,37] Since these are sputtered films, it is also speculated that the first 20−50 nm of the film where the *c*-axis growth has not completely taken over may be partly responsible for the observed thickness dependence of the κ.

Recognizing that film thickness is a main design parameter that determines the resonant frequency of FBARs,[38,39] the film thickness effect[36,37] on the thermal conductivity of $Al_{1-x}Sc_xN$ was investigated in more detail via TDTR measurements to better understand the trends observed in Figure 3a. For this reason, a series of $Al_{1-x}Sc_xN$ films with the thickness range of 50−1000 nm at a fixed composition (x = 0.2) and consistent lateral grain size (~35 nm) were synthesized. Figure 4a shows a noticeable thickness dependence of the cross-plane κ for these $Al_{0.8}Sc_{0.2}N$ films; specifically, κ plateaus for film thicknesses >400 nm and decreases with decreasing thicknesses <400 nm. The turnover in κ near 400 nm, as shown in Figure 4a, implies that there is an appreciable amount of heat being carried by phonons with mean-free paths on this order.[40] As the thickness of the films drops below 400 nm, these phonons begin to scatter at the boundaries with increasing frequency, leading to a continuing reduction in κ as the thickness decreases further. On the other hand, the compositional disorder and grain boundaries reduce κ via scattering of shorter wavelength phonons. Thermal management strategies will therefore be necessary when sub-micron thickness films are integrated into FBAR structures to realize GHz-range resonators.[41]

The implicit nature of thermal effects is further underscored by examining the temperature-dependent thermal conductivity of the thicker $Al_{0.875}Sc_{0.125}N$ and $Al_{0.8}Sc_{0.2}N$ films (765 and 816 nm thick, respectively) over the ambient temperature range of 100−450 K, along with data from 300−450 K for the 733 nm AlN film (Figure 5). Like most crystalline solids, as the temperature is increased beyond 300 K, the thermal conductivity of AlN monotonically decreases because more frequent Umklapp scattering processes[42] cause the phonon mean free paths, and thus the thermal conductivity, to decrease. In contrast, a negligible reduction in κ with increasing temperature is observed for the $Al_{0.875}Sc_{0.125}N$ and $Al_{0.8}Sc_{0.2}N$ films, as shown in TDTR measurement results listed in Figure 5. A similar trend was found in a previous work on $Al_{1-x}Ga_xN$ films with $x = 0.3$ and 0.7.[32]

Given that these temperatures are well below the Debye temperatures of the two constitutive materials,[43,44] the saturation of κ indicates that the increase in heat capacity is balanced—but not overwhelmed by increases in scattering—with temperature. This, in turn, suggests that heat transport is not being dominated by phonon−phonon (i.e., Umklapp) scattering but instead other scattering mechanisms including those discussed so far (grain boundary, film surface, alloy-disorder scattering, etc.).

Finally, thermal conductivity was examined as the $Al_{1-x}Sc_xN$ microstructure was purposely altered by intentionally varying AOG[45] densities for films having a fixed composition ($x = 0.2$) and thickness (∼760 nm). Control of AOG density was realized through incomplete conditioning of the target and chamber combined with incomplete purging of the deposition chamber and load lock. This process keeps the reactive sputter deposition[46] conditions constant while varying the AOG density.[18,33,35] The inclusion of AOGs in $Al_xSc_{1-x}N$ films can dramatically increase the surface roughness in $Al_xSc_{1-x}N$ materials with high Sc content, thus potentially lowering the Q factor of RF microelectromechanical system (MEMS) resonators. Recent reports in the literature demonstrate the significance of the microstructural quality of the base $Al_{1-x}Sc_xN$ film. For example, bulk acoustic wave (BAW) resonators realized in nearly AOG-free $Al_{0.72}Sc_{0.28}N$ films have exhibited an effective k_t^2 of 16% and a Q_{max} of 1070 at 3.5 GHz.[47]

The effect of the AOG is minimal, however, from a thermal perspective. The cross-plane κ is only minimally impacted by the density of AOGs, as shown in Figure 6. The κ of $Al_{0.8}Sc_{0.2}N$ films with varying levels of AOGs were measured using TDTR at room temperature. The qualitative number density of the AOGs is shown in the SEM images (insets) in Figure 6. Despite the fact that the characteristic size of the individual AOGs is on the order of hundreds of nanometers, their density within the majority of the $Al_{1-x}Sc_xN$ matrix remains relatively low. As a result, the rate at which phonons scatter with these AOG interfaces does not impede the total flow of heat carriers to a greater extent than the other scattering mechanisms present. That is, the overall cross-plane κ of the $Sc_xAl_{1-x}N$ films is relatively invariant to the AOG number density. Consequently, while the presence of AOGs in $Al_{1-x}Sc_xN$ is critical for optimizing the electro-acoustic performance of RF MEMS resonators, their impact on thermal transport is observed to be minimal for AOG densities that are low enough to allow the films to be piezoelectrically functional. Scattering mechanisms associated with alloying[30] and the fine crystallite structures (lateral grains; ∼35 nm)[48,49] of the c-axis-textured films dominate (i.e., restrict) the κ. To this end, reduction of the AOG density should not be expected to improve the material's thermal conductivity. However, lower insertion loss associated with minimizing AOG density will result in lower power dissipation within the resonator. Therefore, films with low AOG density will be still beneficial in terms of enhancing the device thermal performance.

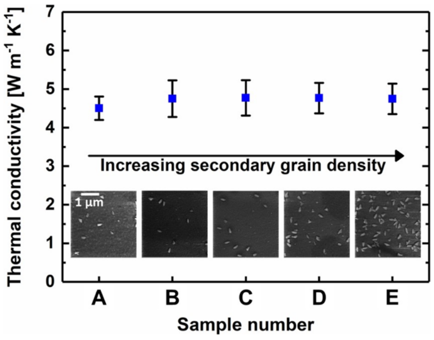

Figure 6. Thermal conductivity of $Al_{0.8}Sc_{0.2}N$ films with varying levels of AOG density. The insets are 75k× SEM images that qualitatively show the increasing AOG density as moving to the right of the x-axis.

2.3. Thermal Modeling Results. A computational study was performed to understand the physical mechanisms driving the FBAR design trade-offs, as they relate to thermal transport, recognizing that composition,[30] film thickness,[36,37] and the fine lateral grain size[48] each contribute to the reduction in the thermal conductivity of $Al_{1-x}Sc_xN$ with respect to the base AlN ($x = 0$) and ScN ($x = 1$) crystals. Ultimately, it was found that the transport mechanisms in these textured (one-dimensionally oriented) films differ from other epitaxial (i.e., three-dimensionally oriented) isostructural wide band gap alloys such as $Al_xGa_{1-x}N$ films.[32] This is because the sputter growth conditions employed lead to close-packed vertically aligned columnar grains which play a significant role in the behavior of phonons and in turn thickness, temperature, and composition trends of the measured thermal conductivity.

In the previous section, thermal conductivity measurements were performed as a function of the ScN composition, film thickness, temperature, and AOG density. These results were analyzed under the paradigm of the phonon gas model leveraging the VCA,[50,51] to assess the comparative importance of the relevant scattering effects on the thermal conductivity of $Al_{1-x}Sc_xN$. The model is in no way prescriptive as the phonon gas model is itself questionable when examining solid solutions.[52] However, it is used here to compare various effects owing to its ease of implementation in a way consistent with decades of previous research.[53]

Practically, the thermal conductivity was modeled using the k-space phonon gas model

$$\kappa = \sum_j \int_0^{\pi/a_{\text{eff}}} \frac{\hbar\omega_j(k)}{6\pi^2} \frac{\mathrm{d}f(\omega_j(k), T)}{\mathrm{d}T} \tau(\omega_j(k), T) v_j^2(k) k^2 \, \mathrm{d}k \tag{1}$$

where ω is the angular frequency, k is the wave vector, a_{eff} is the Debye lattice constant, $\hbar$ is the Planck constant divided by 2π, k_B is the Boltzmann constant, T is the temperature, v is the group velocity, $\mathrm{d}f/\mathrm{d}T$ is the temperature derivative of the Bose−Einstein distribution, and the summation is over the j-dispersion branches. The effective lattice constant, a_{eff}, was calculated by assuming a spherical unit cell where the volume of the sphere is equal to the volume of the real unit cell. Since the measured cross-plane κ is dominated by energy transport along the *c*-axis, a_{eff} was assumed to be equal to the *c* lattice constant (0.498 nm). The total scattering rate, $1/\tau$, was calculated using Matthiessen's rule to sum the contributions from Umklapp scattering, $1/\tau_{\text{U}} = B\omega^2 \exp(-C/T)$, intrinsic impurity scattering, $1/\tau_{\text{I}} = A_0\omega^4$, alloy scattering, $1/\tau_{\text{A}} = x(1 - x)A\omega^4$, boundary scattering, $1/\tau_{\text{B}} = v/d_{\text{film}}$, and grain boundary scattering, $1/\tau_{\text{G}} = v/d_{\text{grain}}$, where x is the ScN fraction, d_{film} is the film thickness, and d_{grain} is the effective grain size. Deduced scattering rate coefficients are presented in Table 2.

Table 2. Scattering Coefficients Obtained by Fitting the VCA Model with Experimental Data

scattering coefficient	value	units
B	1.22×10^{-19}	s
C	290	K
A_0	4×10^{-47}	s^3
A	5.5×10^{-42}	s^3

This model assumes that the dispersion, thermal conductivity, and grain geometries are isotropic. The impact of these assumptions will be discussed in more detail later. Previous studies have shown that dispersion assumptions can have significant effects on thermal predictions.[54,55] Therefore, a full dispersion was used in the model.[56] However, since AlN and ScN possess different crystal structures, wurtzite and rocksalt, it is not possible to average the dispersions in examining the solid solution. Instead, AlN was assumed to act as a host material for Sc impurities. This approximation has shown to be valid when modeling $Al_{1-x}Sc_xN$ optical properties up to $Al_{0.8}Sc_{0.2}N$.[22] However, the elastic constant, C_{33}, significantly softens with alloying, as shown in Figure 3b, leading to significant changes in the maximum phonon frequency and sound speed. This was accounted for by scaling the dispersion, and in turn the velocities, using the ratio of longitudinal velocities predicted from the elastic constants plotted in Figure 3b

$$\frac{v_{\text{L}}(x)}{v_{\text{L}}(0)} = \sqrt{\frac{C_{33}(x)\rho(0)}{C_{33}(0)\rho(x)}} \tag{2}$$

where $v_{\text{L}}(x)$ and $\rho(x)$ are the composition-dependent longitudinal velocity and density, respectively. The mass density $\rho(x)$ of $Sc_xAl_{1-x}N$ was calculated based on the unit cell volume (V) and the molecular weight (M) as a function of the Sc composition, x. The lattice parameters of the wurtzite $Sc_xAl_{1-x}N$ have been reported in ref 57, and the corresponding *a* and *c* values for $x = 0$, 0.125, and 0.2 were extracted via linear interpolation to calculate the unit cell volume. The molecular weight of $Sc_xAl_{1-x}N$ is calculated as $M = xM_{\text{ScN}} + (1 - x)M_{\text{AlN}}$. Finally, the density is calculated using

$$\rho(x) = \frac{ZM(x)}{NV} \tag{3}$$

where Z is the number of molecules per unit cell and N is Avogadro's number. The calculated mass density of $Sc_xAl_{1-x}N$ was 3.24, 3.28, 3.31, and 4.24 g/cm^3 for $x = 0$, 0.125, 0.2, and 1, respectively. It should be noted that experimentally determined ρ_{AlN} and ρ_{ScN} are 3.23[58] and 4.25 g/cm^3,[59] respectively.

Umklapp and intrinsic impurity scattering coefficients were determined by fitting the model to previously reported temperature-dependent AlN thermal conductivity.[60] The AlN films investigated in this work are composed of vertically oriented columnar nano-grains, as shown in Figure 1a−c. The grain boundaries significantly increase scattering, causing these films to exhibit a much lower thermal conductivity than epitaxial AlN.[60] The effective grain size was, therefore, deduced by adjusting the model to fit experimental measurements of this work. This resulted in an effective grain diameter of 70−170 nm, which is much larger than the measured 35 nm. However, the overprediction is consistent since the grains are columnar with a 35 nm diameter and lengths equal to the film thickness (50−1000 nm), and eq 1 assumes isotropic/spherical grains, making the effective grain size larger than the grain diameter. The alloy scattering coefficient was then determined by fitting to the composition-dependent data. The alloy scattering term was forced to be constant between both the thickness and composition series of the $Al_{1-x}Sc_xN$ films. The impact of AOG scattering was neglected since no AOG density dependence was found, as shown in Figure 6.

Figure 3a plots the composition-dependent model for two film thicknesses (d_{film} = ∼125 and ∼750 nm) along with experimental results. It was not possible to fit the composition trend of both thicknesses simultaneously. This is because the effective grain size is not constant with film thickness. As the thickness of the films increases, so does the height of the columnar grains (not the lateral grain diameter), leading to an increase in the effective isotropic grain diameter, d_{grain} (it should be noted that the TDTR and FDTR experiments probed the cross-plane κ values). Therefore, the model predictions shown are for two different grain sizes (d_{grain} = 70 and 170 nm) in the thin (d_{film} = 125 nm) and thick (d_{film} = 750 nm) composition series which fit the experimental results well.

The effect of changing isotropic grain size with film thickness is observed in the thickness-dependent data. Figure 4a plots the film thickness dependence of the κ of $Al_{0.8}Sc_{0.2}N$ films. Below 400 nm thickness, the κ rapidly rises due to boundary scattering of the finite thickness film. Above 400 nm, the conductivity plateaus and becomes thickness independent. It should be noted that for epitaxial GaN films, the thickness dependence was shown to extend into tens of micron thicknesses where the film becomes bulk.[61] The low thickness plateau in this case originates from the grain boundaries taking over as the dominant scattering mechanism for long wavelength, long mean-free path phonons (i.e., Debye-like acoustic modes).

The model is plotted for the two grain sizes (d_{grain} = 70 and 170 nm) used in the composition data to show the impact of grain boundary scattering (Figure 4a). The two grain sizes plotted bound the data above 100 nm thickness since the low film thicknesses have small effective grains. However, as the film thickness increases, the grain length and its effective size increase and approach the 170 nm limit. This hypothesis is further supported since the 50 nm thick films fall below the bound indicating that the effective grain sizes in this case are smaller than 70 nm.

Additionally, Figure 4a suggests that the effective grain sizes of the anomalous composition data point, thick $Al_{0.8}Sc_{0.2}N$ shown in Figure 3a, is smaller than the rest of that series. The thickness-dependent plot is for the 20% Sc composition, which is shown in Figure 3a to not be predicted by the composition trend. Many of the films with thicknesses near 750 nm fall between the 70 and 170 nm bound in Figure 4a indicating a true effective grain size closer to 115 nm. This may suggest that grain size has some composition dependence; therefore, 115 nm grain size was used in the temperature plot of the $Al_{0.8}Sc_{0.2}N$, as shown in Figure 5a.

In addition to the thickness dependence, two sets of data are plotted in Figure 4b to show the effect of residual film stress. The two sets were grown with different substrate bias, leading to a film set with higher levels of compressive stress and a film set with lower levels of compressive stress (Figure 4b). It should be noted that a higher substrate bias leads to films with higher levels of compressive residual stress. These stress values were determined via wafer curvature measurements.[17] Consistently, the films with lower stress have a higher κ. Currently, it is unclear by what mechanism stress impacts thermal conductivity. There are multiple potential ways in which there could be coupling between the average stress state of the film and thermal conductivity. These will be discussed in more detail in a follow-on publication but are introduced briefly here. First, a compressive biaxial in-plane stress could lead to either a change in the N−Al−N bond angle and/or increased out-of-plane (cross-plane) bond length.[62] These factors, in turn, reduce group velocities and increase anharmonicities, resulting in a reduced cross-plane thermal conductivity. Second, changes in stress are often accompanied by changes in the film microstructure. This, in turn, affects the contribution of grain scattering to the effective phonon mean-free path. Third, under energetic bombardment conditions associated with sputter growth (especially with a biased substrate), atomic peening can induce densification of grain boundaries, embed sputter gas atoms, and induce point defects.[63] The latter two would be expected to degrade crystallinity and hence thermal conductivity. Furthermore, if the deposition rate is altered by the factors that influenced the stress state, it should be noted that as the growth rate rises, the concentration of defects also tends to increase. Fourth, it is possible that differences in growth conditions change the propensity for chemical segregation of Al and Sc, which would also modulate the thermal conductivity.

Lastly, the temperature-dependent thermal conductivity for two alloy compositions is plotted in Figure 5a. The thermal conductivity has positive temperature trends until 300 K for both compositions. The VCA model (based on the phonon gas model), on the other hand, predicts a temperature-independent trend above 150 K. First, it should be noted that the experiments were performed under a temperature range below the Debye temperature of $Al_{0.8}Sc_{0.2}N$.[43,44] Therefore, the competing effects of the increase in both heat capacity and Umklapp scattering rate with temperature are influencing the thermal conductivity. Second, this might indicate a strong thermal conductivity contribution from highly localized modes as has been predicted for $In_xGa_{1-x}As$.[52] Third, this trend can be influenced by the grain structure. The films studied in this work are not epitaxial (three-dimensionally oriented) but rather textured (one-dimensionally oriented). We speculate that our model does not properly account for phonon dispersion and scattering associated with the one-dimensional nature[18,54,64,65] of the columnar grains since we assumed an isotropic dispersion, thermal conductivity, and grain geometry.

In summary, the thermal conductivity of $Al_{1-x}Sc_xN$ films can be reasonably predicted by the phonon gas model with the typical alloy, boundary, and phonon−phonon scattering terms. However, its anisotropic grain structure changes with thickness and possibly stress, among other factors, complicating the phonon physics. Therefore, a more rigorous model for these films needs to be developed, in order to properly describe the anisotropic phonon transport and accurately predict thermal conductivity.

3. CONCLUSIONS

This work investigated the physics of thermal transport that governs the thermal conductivity of $Al_{1-x}Sc_xN$, a fundamental building block for 5G RF MEMS. The thermal conductivities of *c*-axis-textured $Al_{1-x}Sc_xN$ films were found to be 1 order of magnitude lower than similarly textured polycrystalline AlN films and 2 orders of magnitude lower than single crystal and/or bulk AlN. This abrupt reduction of thermal conductivity with the incorporation of Sc atoms into the AlN crystal can be understood in terms of phonon-alloy/disorder scattering, in the context of the phonon gas theory. Increasing the Sc composition results in a further decrease in the thermal conductivity due to structural frustration and lattice softening, which is an effect absent in isomorphs such as $Al_{1-x}Ga_xN$. A relatively strong film thickness dependence of the thermal conductivity was observed for the $Al_{1-x}Sc_xN$ films. The $Al_{1-x}Sc_xN$ exhibited a weak temperature dependence beyond room temperature and 450 K. The impact of AOGs on the cross-plane thermal conductivity was found to be negligible for the piezoelectrically functional $Al_{1-x}Sc_xN$ films tested in this work.

Outcomes of this work support the necessity of electro-thermo-mechanical co-design of 5G $Al_{1-x}Sc_xN$-based RF acoustic filters. From a thermal standpoint, for $Al_{1-x}Sc_xN$-based BAW filters, the solidly mounted resonator configuration would be preferred over the FBAR (free-standing membrane) configuration due to the poor thermal conductivity of $Al_{1-x}Sc_xN$. The thermal property data set generated in this work reveals design trade-offs for (i) increasing the Sc composition of $Al_{1-x}Sc_xN$ to maximize the electromechanical coupling factor, (ii) decreasing the film thickness to achieve higher GHz-range resonance frequencies, and (iii) higher operating temperatures resulting from higher integration density and RF input powers. The thermal conductivity data will allow the construction of multi-physics device models that will enable the design and development of $Al_{1-x}Sc_xN$ RF filter technologies with enhanced device performance and improved lifetime.

4. EXPERIMENTAL SECTION/METHODS

4.1. Film Thickness Measurement. Spectroscopic ellipsometry (Woollam M-2000F Focused Beam) was used to measure the thickness of the $Al_{1-x}Sc_xN$ thin films grown on n-type Si(100) substrates. The data were collected in the form of psi (Ψ) and delta (Δ) functions versus wavelength at a fixed angle of incidence of 65°. The three models were used for each $Al_{1-x}Sc_xN$/native SiO_2/Si structured layers, respectively. The ellipsometry measurements were performed in air at room temperature using the wavelength range of 300−1000 nm.

4.2. SEM Imaging. SEM was used to characterize the film microstructure.[66] Imaging was carried out in a MIRA3 (TESCAN USA Inc.) at a working distance of 3 mm and an accelerating voltage of 3 kV to reduce charging. The secondary electrons were collected by the Everhart-Thornley detector. The images were taken at several magnifications, providing a field of view on the sample ranging from 1 to 4 μm. Within these ranges, the microstructure of $Sc_xAl_{1-x}N$ became visible, revealing an oriented grain structure. These grains were measured to be approximately 35 nm across all samples. Some

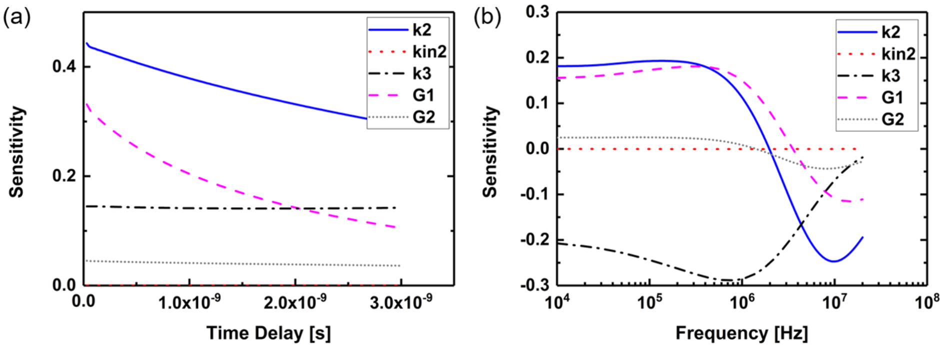

Figure 7. Sensitivity plot for a ∼110 nm thick $Al_{0.875}Sc_{0.125}N$ film measured by (a) TDTR and (b) FDTR. In the legend, $k2$ and $kin2$ are the cross-plane and in-plane thermal conductivities of the $Al_{1-x}Sc_xN$ film, respectively. $k3$ is the thermal conductivity of the Si substrate. $G1$ and $G2$ are the TBCs of the transducer/$Al_{1-x}Sc_xN$ and $Al_{1-x}Sc_xN$/Si interfaces, respectively.

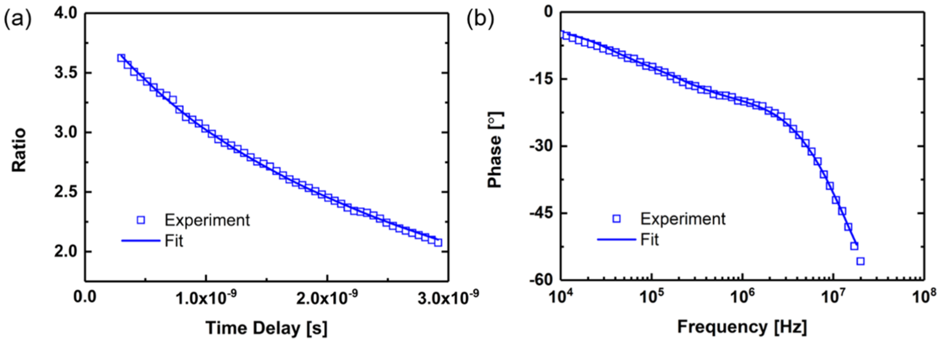

Figure 8. Raw data and fitting results for a ∼110 nm thick $Al_{0.875}Sc_{0.125}N$ film measured by (a) TDTR and (b) FDTR.

misoriented grains (AOGs) were observed, with lateral sizes of 50−250 nm.

4.3. Raman Spectroscopy. Raman spectroscopy was used to characterize changes in optical phonon energies and scattering times with scandium content. All measurements were performed at room temperature using an alpha300R WiTec Raman system employing a 488 nm laser that was focused to a diffraction limited spot by a 100×/0.95 NA laser in a $z(x\text{-})\bar{z}$ scattering geometry. Raman scattered light was dispersed on a 2400 g/mm grating, resulting in a spectral accuracy <0.5 cm^{-1}. To minimize laser heating of the Si substrate, a laser power of 2 mW was used and representative sampling achieved by taking 100 separate spectra evenly spaced over a 100 μm linescan. No significant variation across the film surface was observed. Spectra provided are the composite average of the ensemble of all acquisitions.

4.4. Thermal Conductivity Measurements (TDTR). TDTR is an optical pump−probe method utilizing ultrafast femtosecond laser pulses for measuring the temporal diffusion of heat from the surface down through the bulk over a timescale of 100−5000 ps.[25] The system used in this study is a two-color configuration with a 514 nm pump beam and a 1028 nm probe beam (Flint FL2-12 by Light Conversion, 76 MHz repetition rate, ∼100 fs pulse width). The pump beam is amplitude modulated via an electro-optical modulator at 7 MHz to establish a periodic heating event that can be detected via changes in the thermoreflectance of a thin film metal transducer at the surface through lock-in detection (Zurich Instruments UHFLI). Gold (Au) thin films were deposited as transducers via electron-beam evaporation, and the thickness of the film (81.25 nm) was confirmed via X-ray reflection (XRR) measurements on an Al_2O_3 witness sample. The diameters of the focused pump and probe beams were characterized using a scanning-slit optical beam profiler (Thorlabs BP209-VIS) and were 14 and 9 μm, respectively. Note that these beam sizes are much larger than any lateral variations in the films due to texturing or the presence of AOGs. Literature values were used for the thermal conductivity of Au and Si,[67] as well as volumetric heat capacities (C_V) of Au,[68] AlN,[69] ScN,[44] and Si,[70] where the value of C_V for a particular alloy composition was approximated as a weighted average of the constitutive materials. Fitting of the thermal boundary conductance (TBC) (between the metal transducer and the $Al_{1-x}Sc_xN$ film) and the $Al_{1-x}Sc_xN$ thermal conductivity were performed simultaneously for all samples. As shown in Figure 7, the TBC between the $Sc_xAl_{1-x}N$ film and the Si substrate has little impact on the resulting $Al_{1-x}Sc_xN$ thermal conductivity due to the low measurement sensitivity to this parameter. Measurements were performed on at least three different locations for each sample to account for errors associated with the laser focusing, pump and probe alignment, and potential local variation of the material. The uncertainty was calculated based on 95% confidence bounds for the measurements and a ±2 nm uncertainty in the metal transducer thickness. An identical approach for measurement, fitting, and uncertainty analysis was used in the FDTR experiments, as described below.

4.5. Thermal Conductivity Measurements (FDTR). FDTR measurements of the thermo-physical properties were carried out following deposition of an 80 nm gold (Au) transducer onto the sample surface.[26] The FDTR system uses a pump laser (λ = 405 nm) operating with a 50% duty cycle square wave to heat the Au transducer/sample, while its temperature response is captured from the thermoreflectance signal of a probe laser (λ = 532 nm). The probing wavelength was specifically chosen to maximize the thermoreflectance coefficient of the Au transducer for improved measurement sensitivity. The diameters of the focused pump and probe beams were characterized using a scanning-slit optical beam profiler (Thorlabs BP209-VIS) and were 15.5 and 12.4 μm, respectively. To minimize the uncertainty in the analysis of the FDTR data, the Au transducer thickness was measured by XRR. The $Al_{1-x}Sc_xN$ film thicknesses were determined by using variable angle spectroscopic ellipsometry and cross-sectional SEM. Representative raw data and fitting results for TDTR and FDTR experiments are shown in Figure 8.

AUTHOR INFORMATION

Corresponding Author

Sukwon Choi − *Department of Mechanical Engineering, The Pennsylvania State University, University Park, Pennsylvania 16802, United States;* orcid.org/0000-0002-3664-1542; Email: sukwon.choi@psu.edu

Authors

Yiwen Song − *Department of Mechanical Engineering, The Pennsylvania State University, University Park, Pennsylvania 16802, United States*

Carlos Perez − *Department of Mechanical Engineering, The Pennsylvania State University, University Park, Pennsylvania 16802, United States*

Giovanni Esteves − *Sandia National Laboratories, Albuquerque, New Mexico 87185, United States*

James Spencer Lundh − *Department of Mechanical Engineering, The Pennsylvania State University, University Park, Pennsylvania 16802, United States*

Christopher B. Saltonstall − *Sandia National Laboratories, Albuquerque, New Mexico 87185, United States*

Thomas E. Beechem − *Center for Integrated Nanotechnologies, Albuquerque, New Mexico 87185, United States*

Jung In Yang − *Department of Materials Science and Engineering, The Pennsylvania State University, University Park, Pennsylvania 16802, United States*

Kevin Ferri − *Department of Materials Science and Engineering, The Pennsylvania State University, University Park, Pennsylvania 16802, United States*

Joseph E. Brown − *Electronic Materials and Devices Department, Applied Research Laboratory, University Park, University Park, Pennsylvania 16802, United States*

Zichen Tang − *Department of Electrical and Systems Engineering, University of Pennsylvania, Philadelphia, Pennsylvania 19104, United States*

Jon-Paul Maria − *Department of Materials Science and Engineering, The Pennsylvania State University, University Park, Pennsylvania 16802, United States*

David W. Snyder − *Electronic Materials and Devices Department, Applied Research Laboratory, University Park, University Park, Pennsylvania 16802, United States*

Roy H. Olsson III − *Department of Electrical and Systems Engineering, University of Pennsylvania, Philadelphia, Pennsylvania 19104, United States*

Benjamin A. Griffin − *Sandia National Laboratories, Albuquerque, New Mexico 87185, United States*

Susan E. Trolier-McKinstry − *Department of Materials Science and Engineering, The Pennsylvania State University, University Park, Pennsylvania 16802, United States*

Brian M. Foley − *Department of Mechanical Engineering, The Pennsylvania State University, University Park, Pennsylvania 16802, United States*

Complete contact information is available at: https://pubs.acs.org/10.1021/acsami.1c02912

Author Contributions

Y.S. and C.P. contributed equally to this work. The manuscript was written through contributions of all authors. All authors have given approval to the final version of the manuscript.

Notes

The authors declare no competing financial interest.

ACKNOWLEDGMENTS

This material is based upon work supported by the National Science Foundation, as part of the Center for Dielectrics and Piezoelectrics under grant nos. IIP-1361571, IIP-1361503, IIP-1841453, and IIP-1841466. This work was performed, in part, at the Center for Integrated Nanotechnologies, an Office of Science User Facility operated for the U.S. Department of Energy (DOE) Office of Science. G.E. would like to gratefully thank Sara Dickens and Joseph Michael at Sandia for conducting EBSD analysis. Sandia National Laboratories is a multimission laboratory managed and operated by the National Technology & Engineering Solutions of Sandia, LLC, a wholly owned subsidiary of Honeywell International, Inc., for the U.S. DOE's National Nuclear Security Administration under contract DE-NA-0003525. The views expressed in the article do not necessarily represent the views of the U.S. DOE or the United States Government.

REFERENCES

(1) Nishihara, T.; Yokoyama, T.; Miyashita, T.; Satoh, Y. High performance and miniature thin film bulk acoustic wave filters for 5 GHz. *2002 IEEE Ultrasonics Symposium*, 2002; Vol. *1*, pp 969−972.

(2) Piazza, G.; Felmetsger, V.; Muralt, P.; Olsson, R. H., III; Ruby, R. Piezoelectric aluminum nitride thin films for microelectromechanical systems. *MRS Bull.* **2012**, *37*, 1051−1061.

(3) Akiyama, M.; Kamohara, T.; Kano, K.; Teshigahara, A.; Takeuchi, Y.; Kawahara, N. Enhancement of Piezoelectric Response in Scandium Aluminum Nitride Alloy Thin Films Prepared by Dual Reactive Cosputtering. *Adv. Mater.* **2008**, *21*, 593−596.

(4) Wingqvist, G.; Tasnádi, F.; Zukauskaite, A.; Birch, J.; Arwin, H.; Hultman, L. Increased electromechanical coupling in w−ScxAl1−xN. *Appl. Phys. Lett.* **2010**, *97*, 112902.

(5) Trolier-McKinstry, S.; Zhang, S.; Bell, A. J.; Tan, X. High-Performance Piezoelectric Crystals, Ceramics, and Films. *Annu. Rev. Mater. Res.* **2018**, *48*, 191−217.

(6) Moreira, M.; Bjurström, J.; Katardjev, I.; Yantchev, V. Aluminum scandium nitride thin-film bulk acoustic resonators for wide band applications. *Vacuum* **2011**, *86*, 23−26.

(7) Ruby, R. C.; Bradley, P.; Oshmyansky, Y.; Chien, A.; Larson, J. D. Thin film bulk wave acoustic resonators (FBAR) for wireless applications. *2001 IEEE Ultrasonics Symposium. Proceedings. An International Symposium (Cat. No. 01CH37263)*, 2001; Vol. *1*, pp 813−821.

(8) Kumar, Y.; Rangra, K.; Agarwal, R. Design and Simulation of FBAR for Quality Factor Enhancement. *MAPAN* **2017**, *32*, 113−119.

(9) Griffin, B. A.; Henry, M. D.; Reger, R. W.; Heinz, B. ScxAl1−xN film evaluation using contour mode resonators. *2017 IEEE International Ultrasonics Symposium (IUS)*, 2017; pp 1−4.

(10) Lu, R.; Gong, S. Study of thermal nonlinearity in lithium niobate-based MEMS resonators. *2015 Transducers-2015 18th International Conference on Solid-State Sensors, Actuators and Microsystems (TRANSDUCERS)*, 2015; pp 1993−1996.

(11) Umeda, K.; Kawai, H.; Honda, A.; Akiyama, M.; Kato, T.; Fukura, T. Piezoelectric properties of ScAlN thin films for piezo-MEMS devices. *2013 IEEE 26th International Conference on Micro Electro Mechanical Systems (MEMS)*, 2013; pp 733−736.

(12) Fillit, R.-Y.; Ivira, B.; Boussey, J.; Fortunier, R.; Ancey, P. Structural and thermal investigation for FBAR reliability in wireless applications. *2005 IEEE International Reliability Physics Symposium*, 2005. Proceedings. 43rd Annual., 2005; pp 342−346.

(13) Larson, J. D.; Ruby, J. D.; Bradley, R. C.; Wen, J.; Kok, S.-L.; Chien, A. Power handling and temperature coefficient studies in FBAR duplexers for the 1900 MHz PCS band. *2000 IEEE Ultrasonics Symposium. Proceedings*. An International Symposium (Cat. No. 00CH37121), 2000; Vol. *1*, pp 869−874.

(14) Dubois, M.-A.; Muralt, P. Stress and piezoelectric properties of aluminum nitride thin films deposited onto metal electrodes by pulsed direct current reactive sputtering. *J. Appl. Phys.* **2001**, *89*, 6389−6395.

(15) Mehner, H.; Leopold, S.; Hoffmann, M. Variation of the intrinsic stress gradient in thin aluminum nitride films. *J. Micromech. Microeng.* **2013**, *23*, 095030.

(16) Lee, H.-C.; Lee, J.-Y.; Ahn, H.-J. Effect of the substrate bias voltage on the crystallographic orientation of reactively sputtered AlN thin films. *Thin Solid Films* **1994**, *251*, 136−140.

(17) Knöbber, F.; Zürbig, V.; Heidrich, N.; Hees, J.; Sah, R. E.; Baeumler, M.; Leopold, S.; Pätz, D.; Ambacher, O.; Lebedev, V. Static and dynamic characterization of AlN and nanocrystalline diamond membranes. *Phys. Status Solidi A* **2012**, *209*, 1835−1842.

(18) Henry, M. D.; Young, T. R.; Douglas, E. A.; Griffin, B. A. Reactive sputter deposition of piezoelectric Sc0.12Al0.88N for contour mode resonators. *J. Vac. Sci. Technol., B: Nanotechnol. Microelectron.: Mater., Process., Meas., Phenom.* **2018**, *36*, 03E104.

(19) Loebl, H. P.; Klee, M.; Metzmacher, C.; Brand, W.; Milsom, R.; Lok, P. Piezoelectric thin AlN films for bulk acoustic wave (BAW) resonators. *Mater. Chem. Phys.* **2003**, *79*, 143−146.

(20) Bhugra, H.; Piazza, G. *Piezoelectric MEMS Resonators*; Springer, 2017.

(21) Deng, R.; Jiang, K.; Gall, D. Optical phonon modes in Al1−xScxN. *J. Appl. Phys.* **2014**, *115*, 013506.

(22) Mock, A. L.; Jacobs, A. G.; Jin, E. N.; Hardy, M. T.; Tadjer, M. J. Long-wavelength dielectric properties and infrared active optical phonon modes of molecular beam epitaxy ScxAl1−xN determined by infrared spectroscopic ellipsometry. *Appl. Phys. Lett.* **2020**, *117*, 232107.

(23) Beechem, T.; Graham, S. Temperature and doping dependence of phonon lifetimes and decay pathways in GaN. *J. Appl. Phys.* **2008l**, *103*, 093507.

(24) Kuball, M. Raman spectroscopy of GaN, AlGaN and AlN for process and growth monitoring/control. *Surf. Interface Anal.* **2001**, *31*, 987−999.

(25) Cahill, D. G. Analysis of heat flow in layered structures for time-domain thermoreflectance. *Rev. Sci. Instrum.* **2004**, *75*, 5119−5122.

(26) Schmidt, A. J.; Cheaito, R.; Chiesa, M. A frequency-domain thermoreflectance method for the characterization of thermal properties. *Rev. Sci. Instrum.* **2009**, *80*, 094901.

(27) Braun, J. L.; Hopkins, P. E. Upper limit to the thermal penetration depth during modulated heating of multilayer thin films with pulsed and continuous wave lasers: A numerical study. *J. Appl. Phys.* **2017**, *121*, 175107.

(28) Koh, Y. R.; Cheng, Z.; Mamun, A.; Bin Hoque, M. S.; Liu, Z.; Bai, T.; Hussain, K.; Liao, M. E.; Li, R.; Gaskins, J. T.; Giri, A.; Tomko, J.; Braun, J. L.; Gaevski, M.; Lee, E.; Yates, L.; Goorsky, M. S.; Luo, T.; Khan, A.; Graham, S.; Hopkins, P. E. Bulk-like Intrinsic Phonon Thermal Conductivity of Micrometer-Thick AlN Films. *ACS Appl. Mater. Interfaces* **2020**, *12*, 29443−29450.

(29) David Henry, M.; Young, T. R.; Griffin, B. ScAlN etch mask for highly selective silicon etching. *J. Vac. Sci. Technol., B: Nanotechnol. Microelectron.: Mater., Process., Meas., Phenom.* **2017**, *35*, 052001.

(30) Adachi, S. Lattice thermal conductivity of group-IV and III−V semiconductor alloys. *J. Appl. Phys.* **2007**, *102*, 063502.

(31) Beechem, T.; Christensen, A.; Graham, S.; Green, D. Micro-Raman thermometry in the presence of complex stresses in GaN devices. *J. Appl. Phys.* **2008**, *103*, 124501.

(32) Chatterjee, B.; Lundh, J. S.; Song, Y.; Shoemaker, D.; Baca, A. G.; Kaplar, R. J.; Beechem, T. E.; Saltonstall, C.; Allerman, A. A.; Armstrong, A. M.; Klein, B. A.; Bansal, A.; Seyf, H. R.; Talreja, D.; Pogrebnyakov, A.; Heller, E.; Gopalan, V.; Henry, A. S.; Redwing, J. M.; Foley, B.; Choi, S. Interdependence of Electronic and Thermal Transport in AlxGa1-xN Channel HEMTs. *IEEE Electron Device Lett.* **2020**, *41*, 461.

(33) Talley, K. R.; Millican, S. L.; Mangum, J.; Siol, S.; Musgrave, C. B.; Gorman, B.; Holder, A. M.; Zakutayev, A.; Brennecka, G. L. Implications of heterostructural alloying for enhanced piezoelectric performance of (Al,Sc)N. *Phys. Rev. Mater.* **2018**, *2*, 63802.

(34) Tasnádi, F.; Alling, B.; Höglund, C.; Wingqvist, G.; Birch, J.; Hultman, L.; Abrikosov, I. A. Origin of the Anomalous Piezoelectric Response in Wurtzite ScxAl1-xN Alloys. *Phys. Rev. Lett.* **2010**, *104*, 137601.

(35) Akiyama, M.; Kano, K.; Teshigahara, A. Influence of growth temperature and scandium concentration on piezoelectric response of scandium aluminum nitride alloy thin films. *Appl. Phys. Lett.* **2009**, *95*, 162107.

(36) Cahill, D. G.; Ford, W. K.; Goodson, K. E.; Mahan, G. D.; Majumdar, A.; Maris, H. J.; Merlin, R.; Phillpot, S. R. Nanoscale thermal transport. *J. Appl. Phys.* **2003**, *93*, 793−818.

(37) Majumdar, A. Microscale Heat Conduction in Dielectric Thin Films. *J. Heat Transfer* **1993**, *115*, 7−16.

(38) Park, M.; Hao, Z.; Kim, D. G.; Clark, A.; Dargis, R.; Ansari, A. A 10 GHz Single-Crystalline Scandium-Doped Aluminum Nitride Lamb-Wave Resonator. *2019 20th International Conference on Solid-State Sensors, Actuators and Microsystems & Eurosensors XXXIII (TRANSDUCERS & EUROSENSORS XXXIII)*, 2019; pp 450−453.

(39) Nor, N. I. M.; Ahmad, N.; Khalid, N.; Isa, M. M.; Isa, S. S. M.; Ramli, M. M.; Kasjoo, S. R. The influence of design parameters on the performance of FBAR in 15−19 GHz. *AIP Conf. Proc.* **2018**, *2045*, 20088.

(40) Regner, K. T.; Freedman, J. P.; Malen, J. A. Advances in Studying Phonon Mean Free Path Dependent Contributions to Thermal Conductivity. *Nanoscale Microscale Thermophys. Eng.* **2015**, *19*, 183−205.

(41) Park, M.; Wang, J.; Dargis, R.; Clark, A.; Ansari, A. Super High-Frequency Scandium Aluminum Nitride Crystalline Film Bulk Acoustic Resonators. *2019 IEEE International Ultrasonics Symposium (IUS)*, 2019; pp 1689−1692.

(42) Lv, W.; Henry, A. Non-negligible Contributions to Thermal Conductivity From Localized Modes in Amorphous Silicon Dioxide. *Sci. Rep.* **2016**, *6*, 35720.

(43) Wang, J.; Zhao, M.; Jin, S. F.; Li, D. D.; Yang, J. W.; Hu, W. J.; Wang, W. J. Debye temperature of wurtzite AlN determined by X-ray powder diffraction. *Powder Diffr.* **2014**, *29*, 352−355.

(44) Saha, B.; Acharya, J.; Sands, T. D.; Waghmare, U. V. Electronic structure, phonons, and thermal properties of ScN, ZrN, and HfN: A first-principles study. *J. Appl. Phys.* **2010**, *107*, 033715.

(45) Fichtner, S.; Wolff, N.; Krishnamurthy, G.; Petraru, A.; Bohse, S.; Lofink, F.; Chemnitz, S.; Kohlstedt, H.; Kienle, L.; Wagner, B. Identifying and overcoming the interface originating c-axis instability in highly Sc enhanced AlN for piezoelectric micro-electromechanical systems. *J. Appl. Phys.* **2017**, *122*, 035301.

(46) Wang, D.; Zheng, J.; Tang, Z.; D'Agati, M.; Roebisch, V.; Gharavi, P. S. M.; Liu, X.; Han, M.-G.; Kisslinger, K.; Kratzer, M.; Heinz, B.; Jariwala, D.; Stach, E.; Olsson, R. H., III Ferroelectric C-axis Textured Aluminum Scandium Nitride Thin Films of 100 nm Thickness. *2020 Joint Conference of the IEEE International Frequency Control Symposium and International Symposium on Applications of Ferroelectrics (IFCS-ISAF)*, 2020; pp 1−4.

(47) Moe, C.; Olsson, R. H., III; Patel, P.; Tang, Z.; D'Agati, M.; Winters, M.; Vetury, R.; Shealy, J. B. Highly Doped AlScN 3.5 GHz XBAW Resonators with 16% k2eff for 5G RF Filter Applications. *2020 IEEE International Ultrasonics Symposium (IUS)*, 2020; pp 1−4.

(48) Duquenne, C.; Besland, M.-P.; Tessier, P. Y.; Gautron, E.; Scudeller, Y.; Averty, D. Thermal conductivity of aluminium nitride thin films prepared by reactive magnetron sputtering. *J. Phys. D: Appl. Phys.* **2011**, *45*, 015301.

(49) Pan, T. S.; Zhang, Y.; Huang, J.; Zeng, B.; Hong, D. H.; Wang, S. L.; Zeng, H. Z.; Gao, M.; Huang, W.; Lin, Y. Enhanced thermal conductivity of polycrystalline aluminum nitride thin films by optimizing the interface structure. *J. Appl. Phys.* **2012**, *112*, 044905.

(50) Reid, J. S. Phonon gas. *Phys. Educ.* **1976**, *11*, 348−353.

(51) Nordheim, L. Zur Elektronentheorie der Metalle. I. *Ann. Phys.* **1931**, *401*, 607−640.

(52) Seyf, H. R.; Yates, L.; Bougher, T. L.; Graham, S.; Cola, B. A.; Detchprohm, T.; Ji, M.-H.; Kim, J.; Dupuis, R.; Lv, W.; Henry, A. Rethinking phonons: The issue of disorder. *npj Comput. Mater.* **2017**, *3*, 49.

(53) Chen, G. *Nanoscale Energy Transport and Conversion: A Parallel Treatment of Electrons, Molecules, Phonons, and Photons*; Oxford University Press, 2005.

(54) Mingo, N. Calculation of Si nanowire thermal conductivity using complete phonon dispersion relations. *Phys. Rev. B: Condens. Matter Mater. Phys.* **2003**, *68*, 113308.

(55) Chung, J. D.; McGaughey, A. J. H.; Kaviany, M. Role of Phonon Dispersion in Lattice Thermal Conductivity Modeling. *J. Heat Transfer* **2004**, *126*, 376−380.

(56) Bungaro, C.; Rapcewicz, K.; Bernholc, J. Ab initio phonon dispersions of wurtzite AlN, GaN, and InN. *Phys. Rev. B: Condens. Matter Mater. Phys.* **2000**, *61*, 6720−6725.

(57) Zhang, S.; Holec, D.; Fu, W. Y.; Humphreys, C. J.; Moram, M. A. Tunable optoelectronic and ferroelectric properties in Sc-based III-nitrides. *J. Appl. Phys.* **2013**, *114*, 133510.

(58) Taylor, K. M.; Lenie, C. Some Properties of Aluminum Nitride. *J. Electrochem. Soc.* **1960**, *107*, 308.

(59) Niewa, R.; Zherebtsov, D. A.; Kirchner, M.; Schmidt, M.; Schnelle, W. New Ways to High-Quality Bulk Scandium Nitride. *Chem. Mater.* **2004**, *16*, 5445−5451.

(60) Slack, G. A.; Tanzilli, R. A.; Pohl, R. O.; Vandersande, J. W. The intrinsic thermal conductivity of AIN. *J. Phys. Chem. Solids* **1987**, *48*, 641−647.

(61) Beechem, T. E.; McDonald, A. E.; Fuller, E. J.; Talin, A. A.; Rost, C. M.; Maria, J.-P.; Gaskins, J. T.; Hopkins, P. E.; Allerman, A. A. Size dictated thermal conductivity of GaN. *J. Appl. Phys.* **2016**, *120*, 095104.

(62) Wagner, J.-M.; Bechstedt, F. Properties of strained wurtzite GaN and AlN:Ab initiostudies. *Phys. Rev. B: Condens. Matter Mater. Phys.* **2002**, *66*, 115202.

(63) Abadias, G.; Chason, E.; Keckes, J.; Sebastiani, M.; Thompson, G. B.; Barthel, E.; Doll, G. L.; Murray, C. E.; Stoessel, C. H.; Martinu, L. Review Article: Stress in thin films and coatings: Current status, challenges, and prospects. *J. Vac. Sci. Technol., A* **2018**, *36*, 020801.

(64) Xie, G.; Guo, Y.; Li, B.; Yang, L.; Zhang, K.; Tang, M.; Zhang, G. Phonon surface scattering controlled length dependence of thermal conductivity of silicon nanowires. *Phys. Chem. Chem. Phys.* **2013**, *15*, 14647−14652.

(65) Mingo, N.; Yang, L.; Li, D.; Majumdar, A. Predicting the Thermal Conductivity of Si and Ge Nanowires. *Nano Lett.* **2003**, *3*, 1713−1716.

(66) Zhou, W.; Apkarian, R.; Wang, Z. L.; Joy, D. In *Scanning Microscopy for Nanotechnology. Techniques and Applications*; Zhou, W., Wang, Z. L., Eds.; Springer: New York, 2007; pp 1−40.

(67) Ho, C. Y.; Powell, R. W.; Liley, P. E. Thermal Conductivity of the Elements. *J. Phys. Chem. Ref. Data* **1972**, *1*, 279−421.

(68) Touloukian, Y. S.; Buyco, E. H. Thermophysical properties of matter - the TPRC data series. *Specific Heat—Metallic Elements and alloys. (Reannouncement). Data Book*, 1971; Vol. *4*. at https://www.osti.gov/biblio/5439707.

(69) Mah, A. D.; Weller, W. W.; Christensen, A. U. *Thermodynamic Properties of Aluminum Nitride*. 5716; US Department of the Interior, Bureau of Mines, 1961.

(70) Touloukian, Y. S.; Buyco, E. H. Thermophysical properties of matter - the TPRC data series. *Specific Heat—Nonmetallic Solids. (Reannouncement). Data Book*; IFI/Plenum, 1970; Vol. *5*.